THE TEXAS CESIUM IODIDE ARRAY FOR ASTROPHYSICAL MEASUREMENTS

An Undergraduate Research Scholars Thesis

by

LOGAN JEFFERY

Submitted to the LAUNCH: Undergraduate Research office at
Texas A&M University
in partial fulfillment of the requirements for the designation as an

UNDERGRADUATE RESEARCH SCHOLAR

Approved by
Faculty Research Advisor: Grigory Rogachev

May 2021

Majors: Physics
                                                            Nuclear Engineering

TABLE OF CONTENTS

Page

ABSTRACT

The Texas Cesium Iodide Array for Astrophysical Measurements

Logan Jeffery
Department of Physics and Astronomy
Texas A&M University

Research Faculty Advisor: Grigory Rogachev
Department of Physics and Astronomy
Texas A&M University

A novel cesium iodide detector array has been designed for use at the Cyclotron Institute at Texas A&M University (TAMU). Officially named "The Texas Cesium Iodide Array for Astrophysical Measurements," or TexCAAM, its design is intended for use in sub-Coulomb, alpha-transfer astrophysical experiments. Specifically, TexCAAM was designed to collect data in experiments that offer potential solutions to the Cosmological Lithium Discrepancy, as well as experimental observations of processes that could contribute to the formulation of zero-metallicity, population-III stars in the early Universe. TexCAAM consists of 32 thallium-doped, cesium iodide scintillation detectors that are arranged to surround a mounted target. Its design has high geometric efficiency, possessing a solid angle coverage of $\sim 90\%$. To reduce noise, TexCAAM was designed with a mounted $1500\text{-}\mu$m silicon charged-particle detector that functions as a coincidence gate. Rare isotope beams are available at the TAMU Cyclotron Institute using the Momentum Achromat Recoil Separator. As an efficient gamma spectrometer, TexCAAM can be used to fully characterize the reactions between a beam and a target material.

TexCAAM's construction is complete, and it has undergone energy calibrations for each of its constituent detectors. The efficiency calibration for the array is also complete for low-energy

1

gamma rays (< 1.5-2 MeV). TexCAAM has already been used successfully in several nuclear astrophysical experiments, and final calibrations are currently being conducted to characterize the detector setup for higher energy gamma rays. The physics and methodology for the apparatus characterization are presented in this thesis.

DEDICATION

This work is dedicated to my wife, Maggie, for the encouragement the she provides and the unwavering support that she embodies.

ACKNOWLEDGMENTS

Contributors

I would like to thank my faculty advisor, Dr. Grigory Rogachev, for his guidance and support throughout the course of this project. His brilliant insights and high expectations were vital benefactions to the quality of this thesis. He came up with the idea for TexCAAM and oversaw its completion in weekly group meetings.

I would also like to thank Eric Aboud for his invaluable contribution to this project. Tex-CAAM would not be completed if not for his mentorship and encouragement. TexCAAM is scheduled to be used in many of his current and upcoming projects, and so he played a critical role in its design. Eric wrote the detection analysis code for TexCAAM and led its maiden experiments.

Many others contributed to the research and development of TexCAAM, including Dr. Marina Barbui, Dr. Evgeniy Koshchiy, Dr. Antti Saastamoinen, Dr. Jack Bishop, Karthik Rao, Curtis Hunt, Eric Lester, Dr. Sriteja Upadhyayula, and Dr. Sunghoon "Tony" Ahn. I am incredibly grateful for the help of these individuals.

NOMENCLATURE

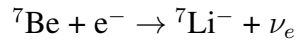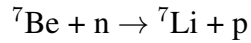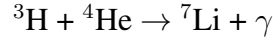|	
^{60}Co	Cobalt-60
ANC	Asymptomatic Normalization Constant
BBN	Big Bang Nucleosynthesis
CNO cycle	Carbon-nitrogen-oxygen cycle
CsI(Tl)	Cesium iodide (tellurium-doped) - generally referred to as simply cesium iodide
HPGe	High-purity germanium detector
$M_\odot$	"Stellar mass" - Equivalent to the mass of the sun
MARS	Momentum Achromat Recoil Separator
PMT	Photomultiplier Tube
Si	Silicon
TAMU	Texas A&M University
TexCAAM	The Texas Cesium Iodide Array for Astrophysical Measurements

1. INTRODUCTION

The Texas A&M Cyclotron Institute houses two cyclotrons that can accelerate ions of low to intermediate energies. The institute takes advantage of the Momentum Achromat Recoil Separator (MARS), which is capable of separating rare-isotope beams that have been accelerated by either the K150 or the K500 cyclotrons [1][2]. In many cases, the reaction between these rare-isotope beams and a target produces gamma-rays which can subsequently be observed via gamma-ray spectroscopy. A novel detector array, referred to as the Texas Cesium Iodide Array for Astrophysical Measurements (TexCAAM), has been constructed to function as an efficient spectrometer to study sub-Coulomb, alpha-transfer events. Alpha-transfer reactions are measured in the lab to simulate alpha-capture reactions that are often seen in astrophysical environments and are associated with some key topics in current research. The two motivations for TexCAAM are found in the Cosmological Lithium Discrepancy and the identification of processes that contribute to ^{12}C production in zero-metallicity stars.

1.1 Cosmological Lithium Discrepancy

It is widely understood that minutes after the Big Bang occurred, primordial nucleosynthesis introduced light nuclei to the ancient Universe, where ^{1}H and ^{4}He constituted over 99% of all nuclei [3]. Small amounts of other nuclei were present post-Big Bang Nucleosyntheses (BBN, as it is commonly referred to), including deuterium (^{2}H), ^{3}He, ^{7}Li, tritium (^{3}H), and ^{7}Be, although tritium and ^{7}Be would shortly decay to ^{3}He and ^{7}Li respectively.

The most widely-accepted models of the Big Bang prove to reflect the observed abundances of many of these early isotopes, with the notable exception of ^{7}Li. These models conclude that three to four times the abundance of ^{7}Li should exist when compared to observational data [4][5]. Outside of BBN, ^{7}Li is also created via several well-known reactions, including:

$$^3\text{H} + {}^4\text{He} \rightarrow {}^7\text{Li} + \gamma$$

$$^7\text{Be} + \text{n} \rightarrow {}^7\text{Li} + \text{p}$$

$$^7\text{Be} + \text{e}^- \rightarrow {}^7\text{Li}^- + \nu_e$$

Models consider these reactions as possible contributors to the expected ^{7}Li abundance. Possible explanations for the Cosmological Lithium Problem tend to fall into one of three categories [5]. A commonly held theory is that the calculations made for the observable abundance of ^{7}Li is incorrect, and systematic errors in detection and decay calculations are to blame for the discrepancy. Another theory is rooted in the incorrectness of the BBN model. Studies have voiced concerns over either an inaccurate attempt to incorporate the strong and weak forces, missing reactions leading to and from ^{7}Li, or a resonance in the triple alpha reaction that formed early stars. Still more believe that the solution is outside of the standard model and, for example, could include dark matter.

TexCAAM is expected to be used in experiments to test the validity of some of the foremost claims that solve the Cosmological Lithium Problem.

1.2 Carbon-12 Development in Population-III Stars

After BBN, light nuclei with masses up through trace amounts of ^{7}Li and ^{7}Be would make up all matter in the Universe. It would not be until about 155 million years after the Big Bang, during the stelliferous era of the early universe, that nuclei larger than ^{7}Li would form [6]. This is because the creation of larger nuclei largely relies on the rare simultaneous collisions between three ^{4}He nuclei, or the triple-alpha process.

More precisely, the triple-alpha process is:

$$^4\text{He} + {}^4\text{He} \rightarrow {}^8\text{Be}$$

$$^8\text{Be} + {}^4\text{He} \rightarrow {}^{12}\text{C} + 2\gamma$$
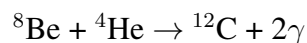
^{8}Be has a half-life on the order of 1×10^{-16} seconds, which is why the reaction is commonly labeled as a "simultaneous" collision of alpha particles. Even after ^{12}C is produced from the

triple-alpha reaction, a rare sequential double-gamma emission (with a branching ratio of 0.04%) is required so it does not decay back into three alpha particles [7]. The frequency of ^{12}C production via triple-alpha reactions relies greatly on the temperature of the star in which the reaction occurs, requiring a temperature of roughly 10^8 K [8]. Because of the rarity of elements larger than ^{7}Li, early stars were made up of light elemental gasses and dust held together by gravity. In massive examples of these zero-metal stars (on the order of M > 100 M$_\odot$), the temperature met the requirements to sustain non-negligible ^{12}C production, although their short lifetimes would not have allowed for the production of much ^{12}C [9][10]. Lower-mass, zero-metal stars could also sustain similar quantities of triple-alpha reactions, but only during their collapse, and the triple-alpha process is not expected to have been frequent enough to sustain itself before it collapsed [11]. In either case, not enough ^{12}C is produced to begin a main-sequence star's well-studied, self-sustaining CNO cycle. The ^{12}C developed during these growth stages would be dispersed upon stellar collapse, meaning that accumulation would have to have occurred over an incredibly long period.

Zero-metallicity stars have yet to be physically observed in space, earning them a category of theoretical population-III (pop-III) stars. Studies regarding the production of early stars often work to describe the production of heavier elements that can better sustain the temperatures and densities required for more-efficient forms of stellar nuclear fusion. Since observation is not possible, terrestrial experimentation is conducted at the low-energy sub-Coulomb level.

1.3 The Texas CsI Array for Astrophysical Measurements

TexCAAM is an assembly of 32 CsI(Tl) scintillator detectors arranged to encompass a large solid angle around a mounted target. Cesium iodide scintillator detectors were used because they were available and have a high density and high gamma-ray attenuation coefficient [12]. A 1500 μm Si detector is placed behind the target to reduce high-energy background noise by acting as a gate via the detection of coincident charged particles. Since gamma-ray ejection is roughly isotropic, this high-solid-angle geometry allows for the highest probability of detection. The compact nature of the assembly creates an environment that minimizes particle loss through the gaps

between the crystals, and therefore contributes to a high geometric efficiency. It was also built in an effort to maintain a consistently high resolution.

This work describes the design and hardware that makes up TexCAAM. Information on the energy and efficiency calibrations are also provided. These calibrations characterize the detector array at low energies, although extrapolating these calibrations to higher energies leads to probable errors in the approximation. In order to accurately describe the detection capabilities at the higher energies seen in experiments, efforts are being made to collect known higher-energy gamma decays from radioisotope beams produced by MARS.

2.   TEXCAAM DESIGN

2.1   The Detector Array

TexCAAM's structure is built around its primary function as a sub-Coulomb reaction gamma detection apparatus. It is made up of 32 CsI(Tl) (hereafter referred to as CsI) scintillation detectors. Although other forms of detectors, including high-purity germanium (HPGe) detectors, could have yielded higher resolutions, common dimensions of HPGe detectors would not have allowed for as high of a geometric efficiency when assembled into a similar array. Furthermore, the CsI crystals and related electronics were already available to the research group at the beginning of this project and are more cost-effective for the intended purpose.

2.1.1   CsI Scintillation

The CsI crystals that make up TexCAAM are a form of scintillator detectors which detect incident photons as they interact with the material. When a photon imparts some or all of its energy to an electron in either the crystal of the the "activator" material within the scintillator crystal lattice (in this case tellurium), the electron moves from its ground state to an excited state [15]. When it decays back to its ground state, subsequent lower-energy photons are released. Scintillators often use photomultiplyer tubes (PMTs) to amplify the energy of the event detected, but the CsI crystals used in TexCAAM are coupled with photodiodes. These photodiodes detect the light emitted from a photon interaction within the crystal and convert it into an electric signal that corresponds to the intensity of the event, or the energy imparted to the scintillation material. Figure 2.1 provides a visual representation of this explanation.
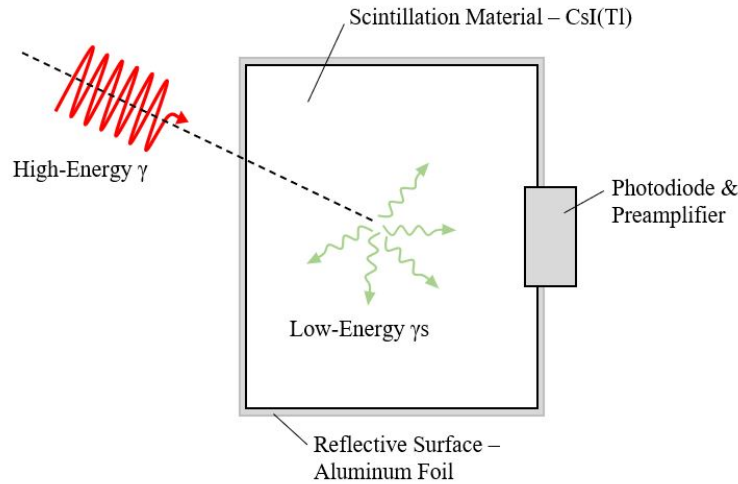
Figure 2.1: Schematic of a CsI scintillation detector with a photodiode and preamp attachment

The CsI detectors used in TexCAAM have been doped with tellurium. This specific type of detector has several added benefits to detection, including relative brightness, a high density, and a high photon stopping power [12]. As scintillators, they also have a short dead time relative to other types of detectors. CsI crystals are mechanically robust and need not be stored in low-moisture or low-temperature environments, as is the case for many similar detectors. The specific detectors used in TexCAAMs assembly are Scionix Holland model # VSOPM40/18-E2-CS-X.

2.1.2 CsI Detector Arrangement

These detectors were assembled and mounted in a 3D-printed frame. Since the 32 crystals weigh a combined 31.8 lbs, the frame was printed using a carbon fiber filament for increased strength and structural rigidity. The frame design includes windows for access to the connection ports located on the back of each of the crystals. The carbon fiber box was mounted on a separate 3D-printed stand so that the bottom CsI crystals were also accessible, and a 3D-printed halo was added to the top of the frame to keep the detector frame assembly together. Figure 2.2 shows the assembled detectors along with the 3D printed frame, stand, and halo.
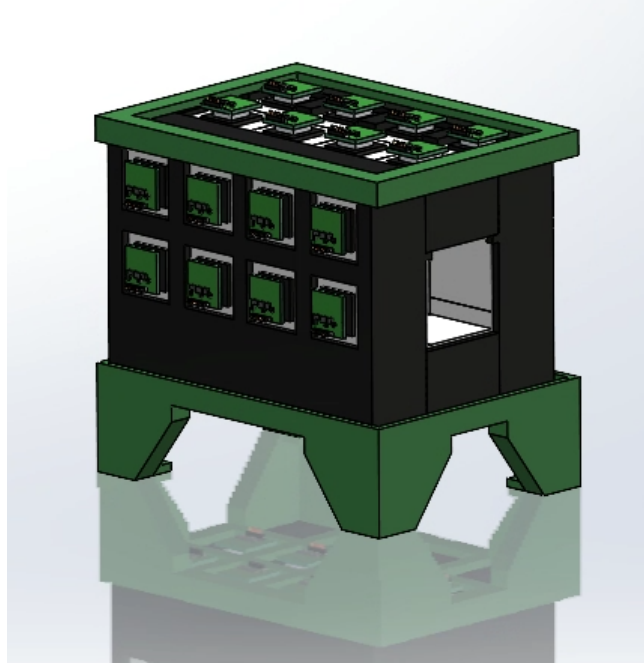
Figure 2.2: CsI detector assembly and frame modelled with SolidWorks

It should be noted that other geometries were considered for the detector assembly, including a typical hexagonal configuration. This final assembly was chosen because it features the highest solid angle from the centrally-mounted target, and also considers the expectation that Compton-scattered gamma rays will pass through gaps between loosely-organized scintillation detectors. Since photon interactions with the detectors can occur anywhere within the crystals, it is desired to have the highest available thickness through which a photon would have to traverse.

2.2 The Target Arm

MARS separates rare-isotope beams which can then be directed down a beam line towards a target. TexCAAM takes advantage of this by including a custom "target arm" that connects to and acts as a continuation of the beam line. This target arm runs through the opening in the TexCAAM detector assembly. A separate target mount holds the thin target material and slides into the target arm such that the interactions between the target and the beam occur at the center of the CsI assembly.
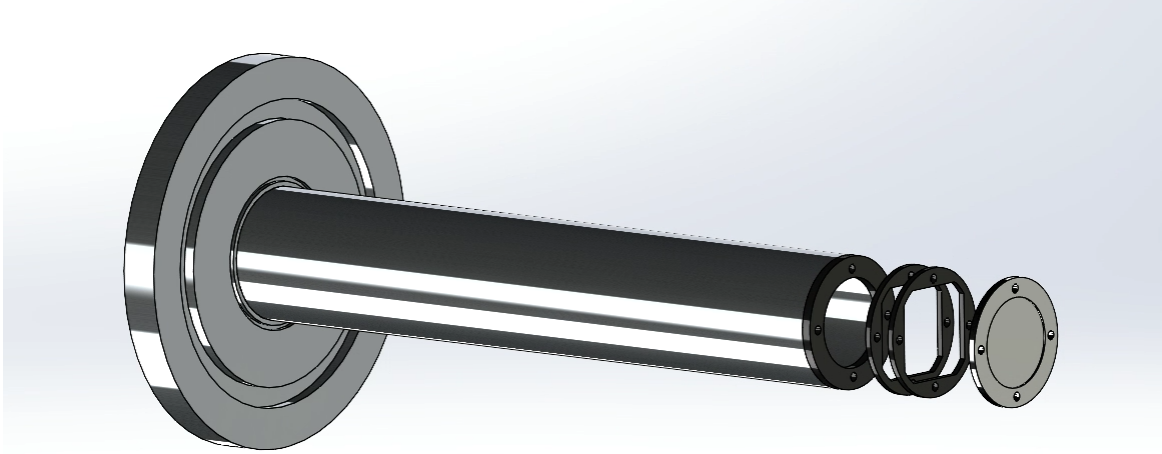
Figure 2.3: TexCAAM's target mount with the target mount attachments and silicon detector

A silicon wafer detector is also used as part of a gate that reduces noise from background radiation. It detects charged-particle products that are emitted from the interactions with the target. It then opens a time window for which associated gamma-rays can be detected and registered by the CsI detectors. The particular silicon detector used in TexCAAM is a Micron MSD026 circular single-area detector. It is 1500 μm in thickness, and was chosen for its ability to stop most deuterons produced from a 10 MeV beam of ^{7}Be via the ^{7}Be(^{6}Li,d) reaction.

Depending on the experiment, the silicon detector can be backed by an array of plastic scintillators that act as a veto for all particles that pass through the silicon detector undetected. This often includes light charged particles like protons.

2.3 Other Assembly Components

2.3.1 The Aluminum Box

The 3D printed detector frame screws into a 1/2" aluminum base plate, off of which is a fully-encapsulating aluminum box that acts as a light shield to reduce noise. Within the box, two circuit boards have been mounted to the base plate where output from each of the CsI detectors is connected. These signals are fed via ribbon cables through a transition board at the top of the

aluminum box. The transition board has a light-tight connection and feeds the signals from the detectors to three digitizers.
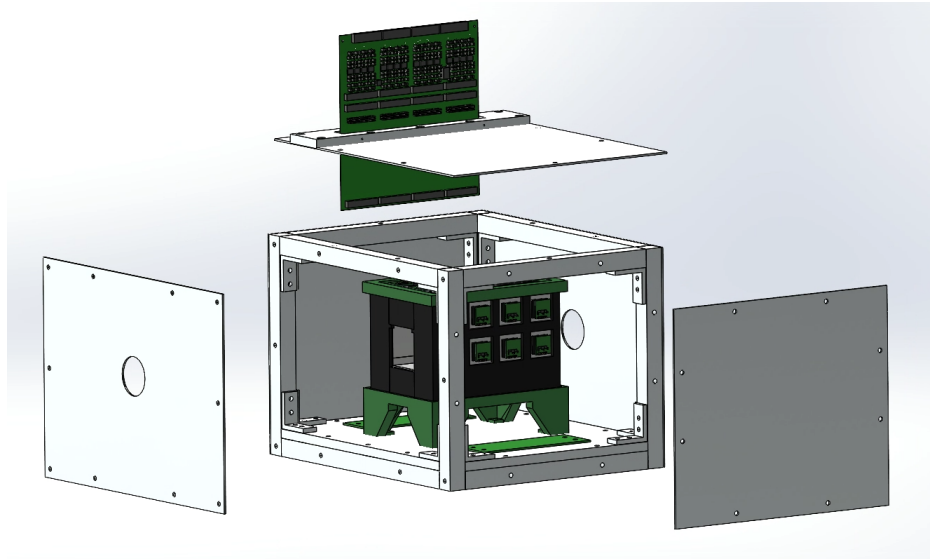
Figure 2.4: The CsI array and frame within the light-tight aluminum box modelled in SolidWorks
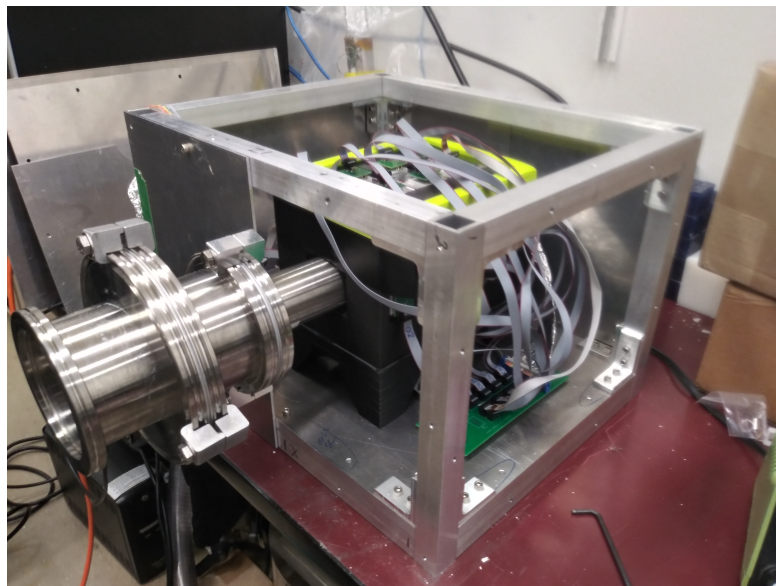
Figure 2.5: Detector assembly and electronics within the open aluminum box

Figure 2.6: Detector assembly and electronics within the closed aluminum box

The electronic connections are represented by the block diagram provided as Figure 2.7. Of course, this connection scheme depends on the conditions of the experiment. For the ^{60}Co calibrations which are discussed in the next section, a Si detector was not used. Therefore, this meant a simple setup featuring a single line of connection between the CsI detectors and the digitizers. The digitizers have an internal trigger for the CsI detectors.
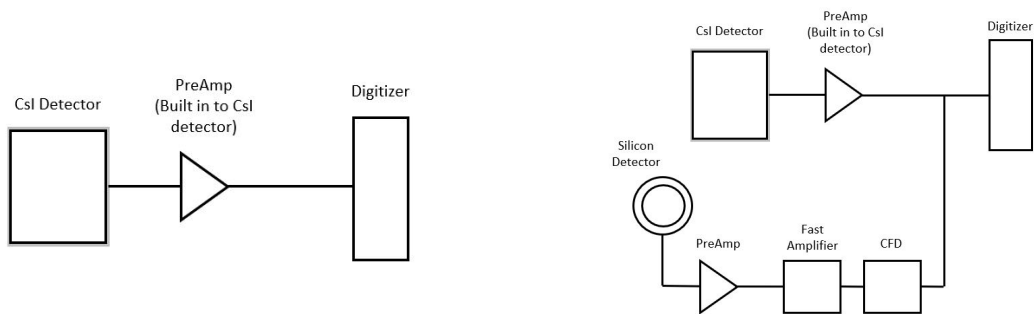
Figure 2.7: (Left) Detector setup used for the calibrations (Right) A potential detector setup that includes both the CsI detector array and the silicon detector gate

For further reduction to the background interactions with the CsI crystals, the entire aluminum box is surrounded in 2"- thick lead bricks. The combined weight of TexCAAM and the lead bricks is over 1700 lbs, necessitating a separate support structure that could allow TexCAAM to mount to MARS. Aluminum was used because it was light, inexpensive, and available. This stand was build so that TexCAAM would sit at a 5° incline. This is to match the angle of incline from MARS, which was designed to optimize the transmission of the radioactive ion beam. The dimensions of the stand account for the size of the lead blocks which are to be used as shielding. These are generally 8" × 4" × 2".
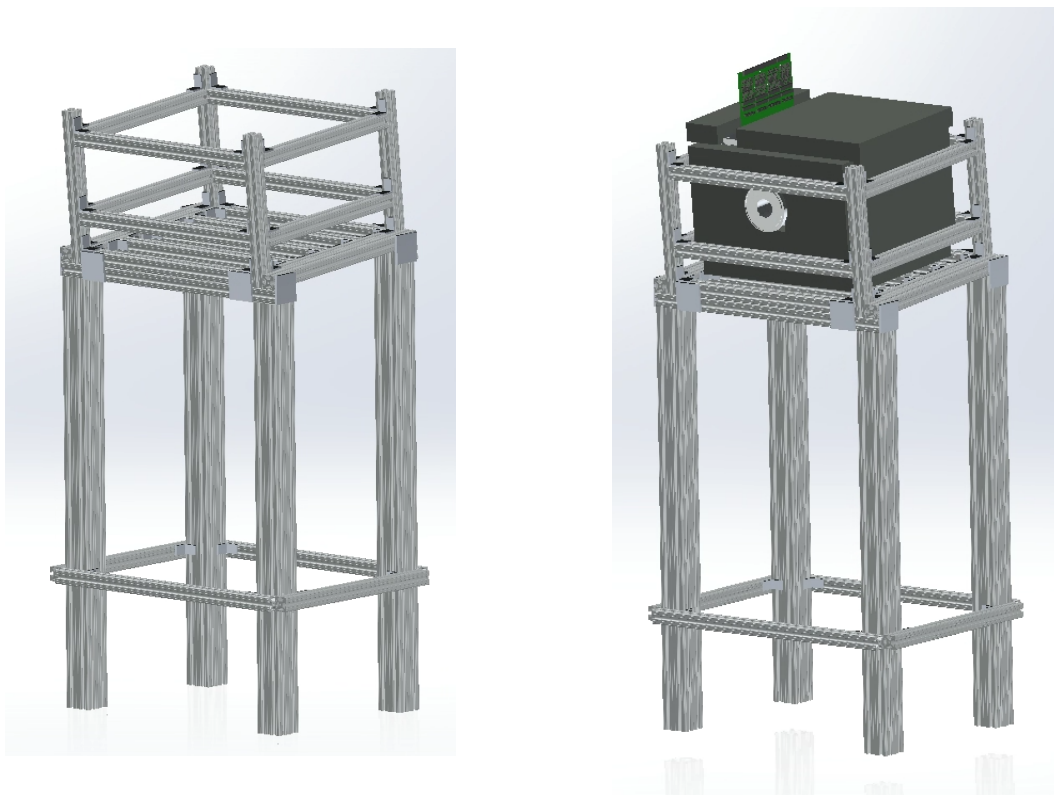
Figure 2.8: TexCAAM's stand with (left) and without (right) the detector array and lead shield
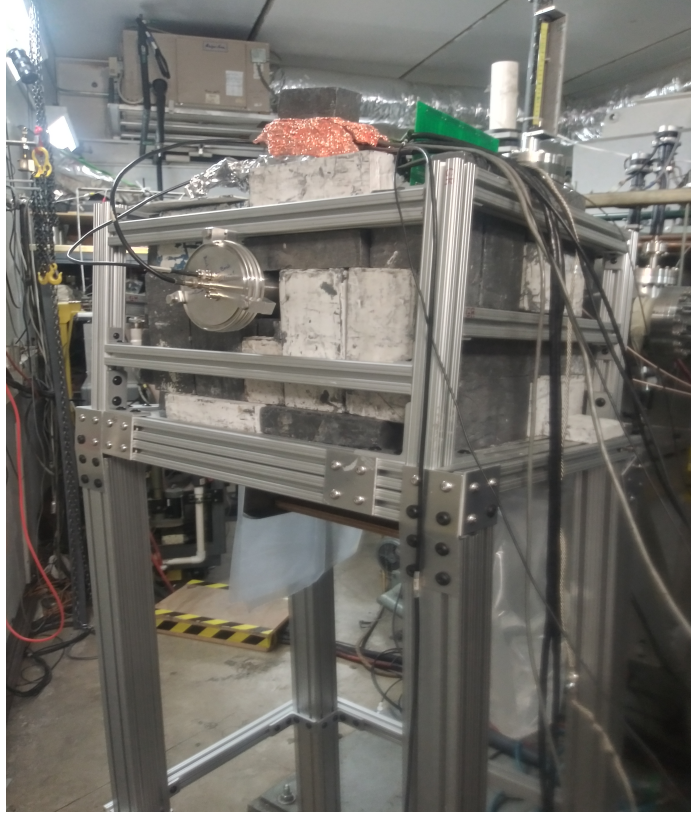
Figure 2.9: TexCAAM as prepared and shielded for use in experimentation. Pictured as attached to the MARS beamline.

3. DETECTOR CHARACTERIZATION

To fully characterize TexCAAM's detection capabilities, energy and efficiency calibrations were performed using a ^{60}Co gamma source. ^{60}Co was used because it follows a well-known decay scheme; it beta-decays to ^{60}Ni with a branching ratio of 0.9988 and then subsequently releases energy in a cascade of two near-simultaneous (within 8×10^{-13} seconds) photon emissions [13]. These photon energies (1.173 MeV and 1.333 MeV) are often used as reference points to calibrate detector setups.
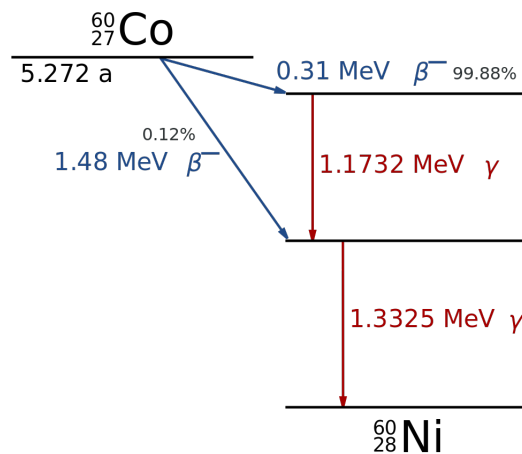
Figure 3.1: ^{60}Co decay scheme [14]

3.1   Energy Calibration

The amplitude of the signal produced by the detected and produced by a scintillator detector is directly proportional to the energy deposited by that reaction. A simple linear channel-to-energy calibration was performed on the TexCAAM assembly using a ^{60}Co gamma source. This calibration uses two reference points for the linear channel-to-energy fit, consisting of both of the photon energy peaks. It excludes a 0 MeV to channel 0 assumption. These energy calibrations were

performed on each individual detector. Data for each detector is provided in the appendix, and a visualization of the linear fit for "Detector 1" is provided in Figure 3.2.
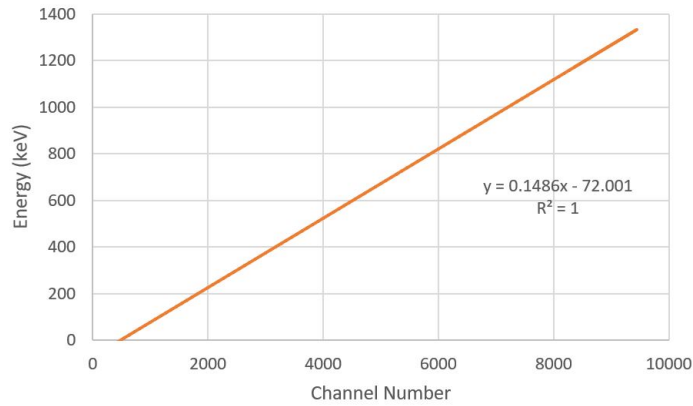
Figure 3.2: Detector 1 energy calibration using a ^{60}Co source

This method of calibration only serves as an approximation. It is an inaccurate assumption that scintillators detect events linearly with energy. It is understood that scintillators are more efficient at detecting lower-energy photons because the scintillation material has a higher photoelectric absorption probability at low energies. Here, the probability of photoelectric absorption scales at roughly $E^{-3.5}$.

Since this apparatus will typically be used in gamma-collection of up to 7-8 MeV, there is expected error with this linear assumption. The relative closeness that the two ^{60}Co decay peaks have compared to the measuring range contributes to the error as the error over this short range will be magnified.

There are plans to improve the energy calibrations of these detectors that include collecting data from a higher-energy incident beam on a target that produces detectable photons with known energy. This will provide a third point at a larger energy that will consequentially reduce the error in the calibration.

3.2 Efficiency Calibration

The assembly's geometric efficiency is estimated to be the ratio of the total solid angle covered by a detector from the target. This can easily be calculated using Eq. 1. Here, θ and ϕ are used to describe the projection of a shape onto a sphere centered at the target.

$$\Omega = \iint_S \frac{\hat{r} \cdot \hat{n}}{r^2} dS = \iint_S \sin(\theta) d\theta d\phi \qquad \text{(Eq. 1)}$$

It was determined that the apparatus has a target-to-detector face solid angle of around 90%. This calculation makes the assumption that all photon-detector interactions will take place on the surface of the detectors. This is not true, as the probability of interaction (i.e. detection) is dependent on the distance traversed through the material. This formulation for the geometric efficiency, however, does provide some insight on what can be expected when performing a more-thorough efficiency calibration.

At energies consistent with the decay peaks of ^{60}Co, the cross-section for photoelectric absorption and Compton scattering events in CsI dominate with a negligible probability for pair production. Figure 3.3 shows this.
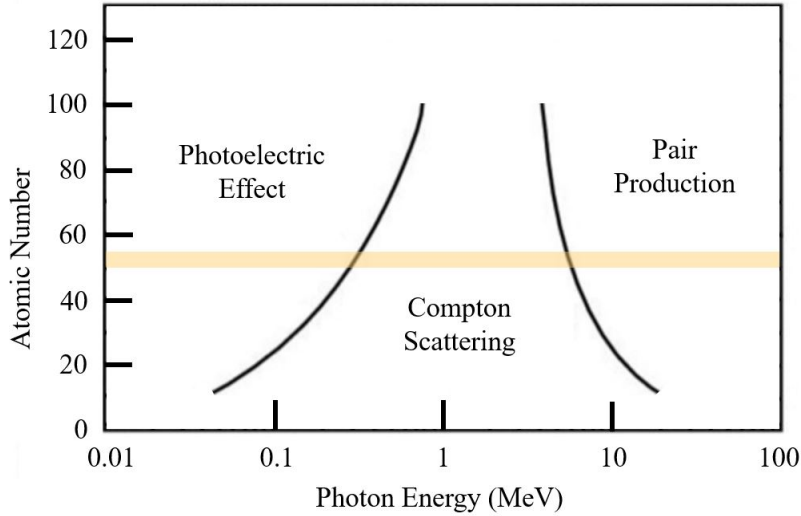
Figure 3.3: Photon interactions as a function of energy level and absorbing material [16] where the range for CsI absorption is highlighted

Efficiency in a broader sense quantifies the expected amount of events detected by the detection apparatus compared to the total number of decays in the ^{60}Co source. Total efficiency of a detector or system of detectors is found as the product of the geometric and intrinsic efficiencies. In the case of TexCAAM, direct calculation of the total efficiency is impossible since the ^{60}Co source has no identifying activity information that could tie it to a calibrated activity at a specific date. This would have allowed for a simple calculation using the elapsed time (t) and half-life (λ) of ^{60}Co to determine an ideal detection rate for comparison, namely

$$A = A_0 \cdot e^{-\lambda t} \tag{Eq. 2}$$

Rather than basing the decay rate off of source calibration information, the detection apparatus can be calibrated by the detection frequency of the two peaks alone. Since detecting one photon (of either energy) implies the emission of the second, the efficiency can simply be calculated as the ratio of the number of events in which both corresponding photons were detected to the total number of either 1.1 MeV or 1.3 MeV photons detected. The efficiency should ideally

21

be independent of the peak used in the denominator of this ratio, although in practice, it is under-stood that higher-energy photons are less likely to be absorbed in the scintillation material. The following equations show this process.

$$N_{1.1} = A \cdot t \cdot \epsilon(E_{1.1})$$
$$N_{1.3} = A \cdot t \cdot \epsilon(E_{1.3})$$

Here, $N_{1.1}$ and $N_{1.3}$ are the number of detected 1.1 MeV and 1.3 MeV events respectively, A is the activity of the ^{60}Co gamma source, t is the time of collection, and ϵ is the efficiency at a given energy. A formulation for the net efficiency could therefore be independent of the activities and duration of collection, as seen in Eq. 3.

$$N_{1.1 \ \& \ 1.3} = A \cdot t \cdot \epsilon(E_{1.1}) \cdot \epsilon(E_{1.3}) = N_{\text{tot}} \cdot \epsilon(E_{1.1}) \cdot \epsilon(E_{1.3})$$

$$N_{1.1} = N_{\text{tot}} \cdot \epsilon(E_{1.1})$$

$$\epsilon(E_{1.1}) = \frac{N_{1.1 \ \& \ 1.3}}{N_{1.3}} \tag{Eq. 3}$$

Since the two ^{60}Co decays occur within 8×10^{-13} s, this is well-within the nanosecond time scale of the detectors. The events can therefore be considered "simulataneous" for the purpose of this efficiency calibration.

Determining the efficiency of a single detector is fairly straightforward, as it requires no more than simple calculations based off of a single spectrum. In order to obtain the efficiency resolution across multiple detectors, however, the time delay between any two detectors must be known. The property of simultaneity between the ^{60}Co gamma emissions is used to find the delay between a detector and any other detector. This delay is not necessarily identical for each detec-tor, although the location of the detectors relative to each other is inconsequential as the distance between the furthest detectors in the array is less than one light-nanosecond. The delay between detectors may be influenced somewhat by the detection speed of the electronics setup. The delay

time can be found by subtracting time vs event count data from similar data in another detector. Since the angular correlation between these two decays peaks only slightly at 180 degrees [13], an upper-triangular matrix of time delays between all the detectors has been generated. All pertinent delay times have been included in the appendix, and an example histogram used to identify the delay time between detectors "2" and "4" is shown in Figure 3.5. The average time delay between detectors is 28.9 ns (Figure A.4).
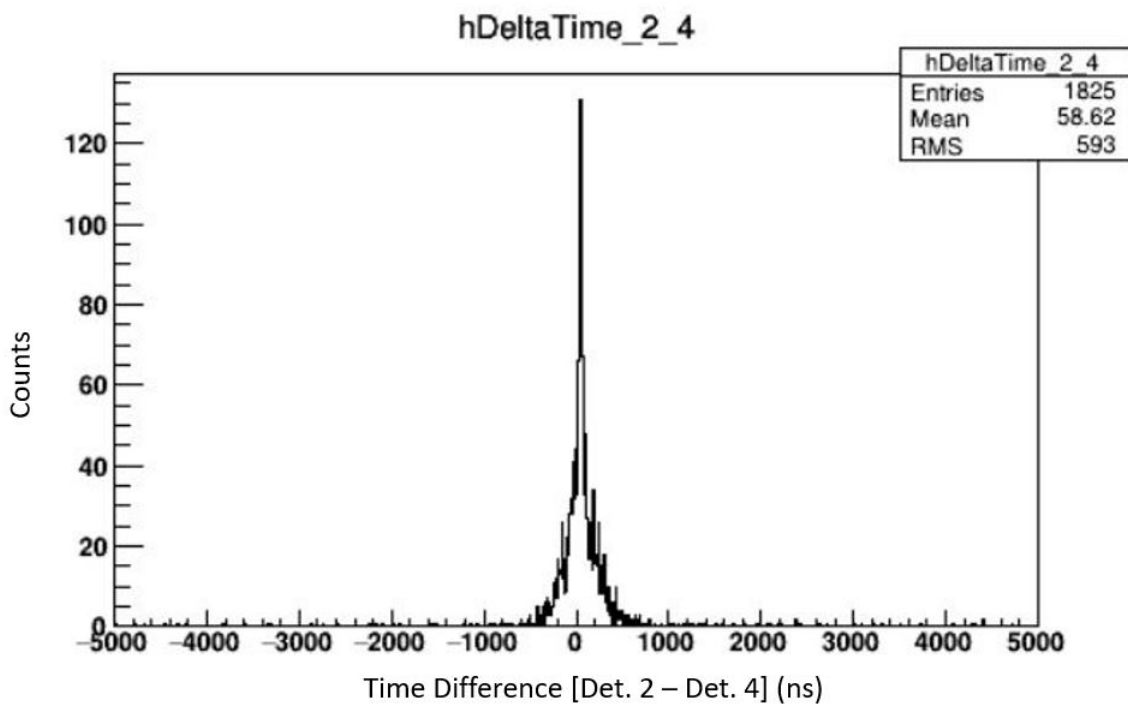
Figure 3.4: The delay time between CsI detectors 2 and 4

Furthermore, the appendix also includes a matrix that identifies the counts constituting each of the time delay peaks. By summing each of these peak areas, the total number of instances in which both of the 1.1 MeV and 1.3 MeV events were detected is found to be $N_{1.1 \ \& \ 1.3} = 2.67 \times 10^6$. By fitting the aggregate data from each of the 32 crystals, the area of the individual energy peaks is found to be $N_{1.1} = 7.537(42) \times 10^6$ and $N_{1.3} = 6.024(14) \times 10^6$. These values differ somewhat,

23

which is likely a result of the linear background fit that was applied.
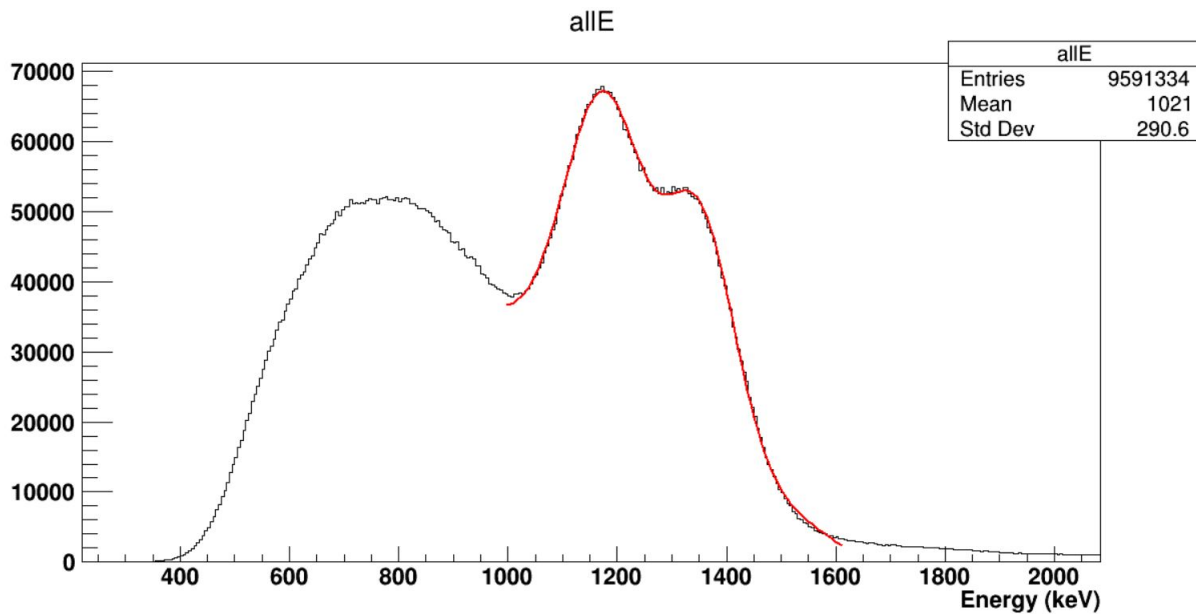
Figure 3.5: A spectrum generated from the data collected by all 32 CsI detectors and an associated double-peak fit

According to Eq. 3, the total efficiency of the detection system is found to be $\epsilon_{1.1} = 0.4432(1)$ or $\epsilon_{1.3} = 0.3543(2)$, where $\epsilon_{1.1}$ and $\epsilon_{1.3}$ differ by $\sim 21\%$.

3.3 Energy Resolution Issues

The theoretical best resolution for the setup is estimated to be around 7-8% at an energy of 1.1 MeV [15]. This comes from the error in the expected counting statistics, and the realistic assumption that many photons will pass undetected due to losses at the boundaries, in the photodiodes, and in the crystals themselves. The summed histogram presented as Fig. 3.5 presents a resolution of roughly 13% (12.5% or 14.6%- depending on the peak). The data collection was replicated in a reduced noise environment and confirmed these results. This less-than-ideal resolution was the result of intrinsic deficiencies in some of the detectors - namely that their gain is insufficient to produce high-resolution statistics. This low gain is likely caused by a combina-

tion of small tears in the reflective surface, possible photodiode misplacement or malfunction, and increased crystal opacity caused by years of use. These issues would have driven up the noise-to-signal ratio and decreased the overall resolution.

To decrease the noise-to-signal ratio and improve resolution, a stronger ^{60}Co source could be used. Furthermore, corrections to the previously listed detector deficiencies would yield a higher gain, and higher-energy gamma collection would improve the accuracy of the calibrations.

4. CONCLUSION

TexCAAM features several unique and beneficial traits that make it suitable for sub-Coulomb astrophysical experimentation, including a low-energy efficiency of approximately 40%, $\sim 90\%$ solid angle coverage, and compatibility with the TAMU Cyclotron Institute's MARS radioisotope beam generator. Its construction and implementation will hopefully shed light on several key issues in nuclear astrophysics.

This work presents a full detection characterization for the TexCAAM CsI assembly conducted with an unknown ^{60}Co source. The energy calibration shows a linear fit between the two decay peaks. The efficiency calibration uses the observed simultaneity of the two gamma emissions to determine the efficiency at the 1.1-1.3 MeV range for the entire detector array. Collection and analysis of a higher-energy spectrum would improve the calibration accuracies. Moreover, improvements can be made to the CsI detectors themselves to further increase the energy resolutions. During experimentation, the inclusion of the silicon detector gate will significantly reduce noise from high-energy cosmic background radiation.

REFERENCES

[1] Tribble, R., Azhari, A., Gagliardi, C., Hardy, J., Mukhamedzhanov, A., Tang, X., . . . Yennello, S. (2002). Radioactive beams at Texas A&M University. Nuclear Physics A, 701(1-4), 278-281. doi:10.1016/s0375-9474(01)01597-4

[2] Tribble, R., Burch, R., &; Gagliardi, C. (1989). MARS: A momentum achromat recoil spectrometer. Nuclear Instruments and Methods in Physics Research Section A: Accelerators, Spectrometers, Detectors and Associated Equipment, 285(3), 441-446. doi:10.1016/0168-9002(89)90215-5

[3] Peebles, P. J. (1966). Primeval helium abundance and the primeval fireball. Physical Review Letters, 16(10), 410-413. doi:10.1103/physrevlett.16.410

[4] Hou, S. Q., et. al. (2017). "Non-extensive statistics to the cosmological lithium problem". The Astrophysical Journal, vol. 834, pp. 165.

[5] Fields, B. D. (2011). "The primordial lithium problem". Annual Review of Nuclear and Particle Science. 61: 47–68.

[6] Coc, Alain; Vangioni, Elisabeth (2014). "Revised Big Bang Nucleosynthesis with long-lived negatively charged massive particles: Impact of new 6Li limits, primordial 9Be nucleosynthesis, and updated recombination rates". arXiv:1403.4156v1 [astro-ph.CO].

[7] Hoyle, F. (1954). "On Nuclear Reactions Occurring in Very Hot Stars. I. the Synthesis of Elements from Carbon to Nickel". The Astrophysical Journal Supplement Series. 1: 121. Bibcode:1954ApJS....1..121H. doi:10.1086/190005. ISSN 0067-0049.

[8] C. Angulo, M. Arnould, M. Rayet, P. Descouvemont, D. Baye, C. Leclercq-Willain, A. Coc, S. Barhoumi, P. Aguer, C. Rolfs, R. Kunz, J. W. Hammer, A. Mayer, T. Paradellis, S. Kossionides, C. Chronidou, K. Spyrou, S. Degl'Innocenti, G. Fiorentini, B. Ricci, S. Zavatarelli, C.

Providencia, H. Wolters, J. Soares, C. Grama, J. Rahighi, A. Shotter, and M. Lamehi Rachti, "A compilation of charged-particle induced thermonuclear reaction rates," Nuclear Physics A, 1999.

[9] P. Marigo, L. Girardi, C. Chiosi, and P. R. Wood, "Zero-metallicity stars I. Evolution at constant mass," Astronomy and Astrophysics, vol. 371, pp. 152–173, 2001.

[10] V. Bromm and R. B. Larson, "The First Stars," Annual Review of Astronomy and Astrophysics, vol. 42, no. 1, pp. 79–118, 2004.

[11] N. Christlieb, M. S. Bessell, T. C. Beers, B. Gustafsson, A. Korn, P. S. Barklem, T. Karlsson, M. Mizuno-Wiedner, and S. Rossi, "A stellar relic from the early milky way," Nature, vol. 419, no. 6910, pp. 904–906, 2002.

[12] Grassmann, H., Lorenz, E., &; Moser, H. (1985). Properties of CsI(TI) — Renaissance of an old scintillation material. Nuclear Instruments and Methods in Physics Research Section A: Accelerators, Spectrometers, Detectors and Associated Equipment, 228(2-3), 323-326. doi:10.1016/0168-9002(85)90276-1

[13] Muhlberger, Curran D. "Experiment IX: Angular Correlation of Gamma Rays." University of Maryland, College Park. May 9, 2008.

[14] Inductiveload, Public domain, via Wikimedia Commons. https://commons.wikimedia.org/wiki/File:Cobalt-60_Decay_Scheme.svg

[15] Knoll, G. F. (2020). Radiation Detection and Measurement (4th ed.). S.l.: JOHN WILEY.

[16] Cherry, S. R., Sorenson, J. A., &; Phelps, M. E. (2012). Physics in Nuclear Medicine. Philadelphia, PA: Saunders.

APPENDIX
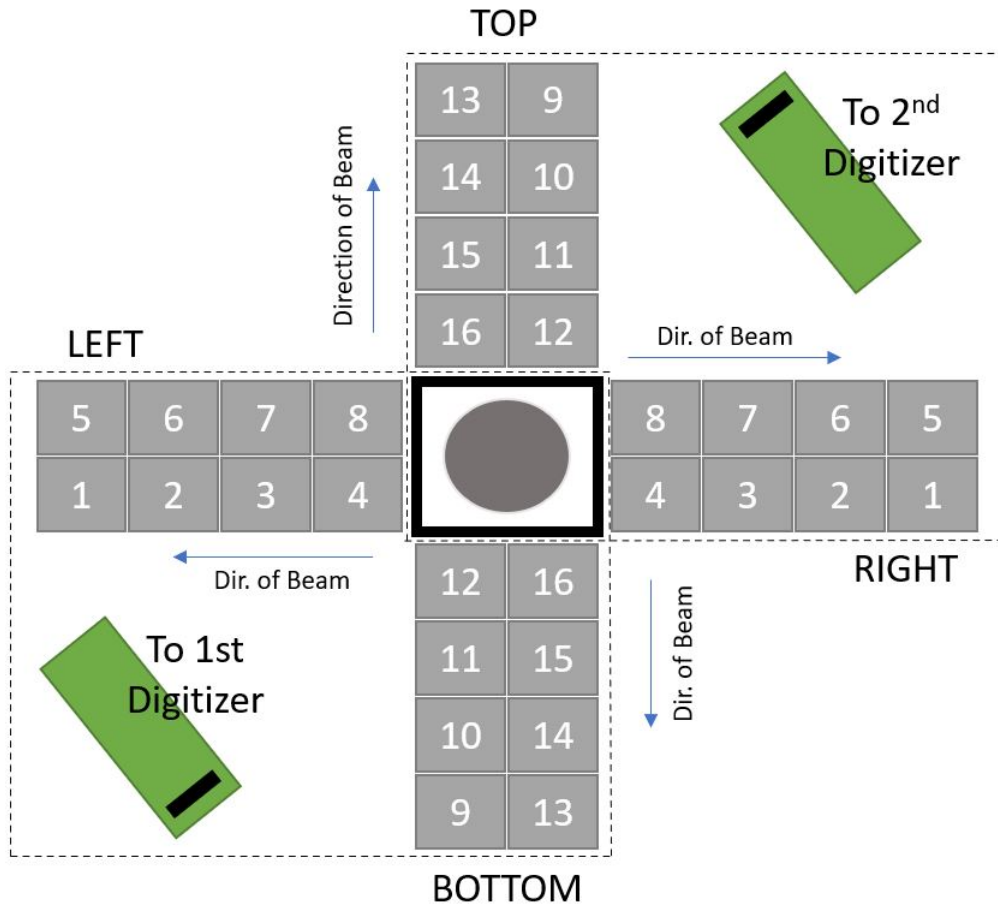
Figure A.1: Schematic of the CsI detector arrangement in TexCAAM

Table A.1: Energy calibration using ^{60}C source for each of the 32 CsI detectors

CsI #	1173	1332	Sum Peak (2505)	CsI #	slope	y
1	8379.47	9449.51	18133.5	1	0.136029	39.8326
2	8489.23	9602.29	17648.2	2	0.145608	-64.1879
3	10099.9	11447.1	21284.9	3	0.119179	-31.071
4	9843.38	11136.6	20961.7	4	0.119682	-2.74214
5	10731.9	12201.9	23452.6	5	0.104572	53.5722
6	8552.03	9879.1	18772.6	6	0.130935	46.7232
7	10477.5	11892.6	22358.1	7	0.112137	-1.41893
8	8511.39	9736.15	18206.5	8	0.137832	-4.3692
9	9189.06	10435.3	20055.9	9	0.122365	51.9823
10	9766.33	11059.4	20622	10	0.122725	-25.0752
11	8015.12	9366.4	17640	11	0.139624	40.5304
12	9246.65	10557.3	19565.2	12	0.129542	-29.5012
13	8745.66	9919.63	18470.7	13	0.137086	-26.4609
14	12505	14213.1	27226.8	14	0.090376	45.3716
15	11620.3	13337.1	24773.6	15	0.101769	-16.5473
16	11312.6	12891	23641.3	16	0.108465	-59.3572
17	11274.9	12845	22697.8	17	0.117511	-163.387
18	9851.25	11192	21339.1	18	0.115852	33.787
19	10642	12083.5	22509.1	19	0.112377	-23.9657
20	9357.07	10624	19753.9	20	0.12829	-28.7193
21	9224.03	10706.8	20471	21	0.119082	66.7674
22	11561.4	13113.5	25037.7	22	0.0986924	35.0621
23	10646.3	12057.5	22471.3	23	0.112676	-26.2296
24	9613.65	10892.3	20357.8	24	0.123993	-18.4607
25	10691.7	12130.5	22773.2	25	0.110272	-5.47994
26	10774.6	12219	23263.9	26	0.106514	28.1259
27	9941.12	11224.3	20961.7	27	0.12075	-25.1333
28	11985.5	13862.4	26358.7	28	0.093134	49.7437
29	12528.8	14317.7	27566.4	29	0.0885895	63.6761
30	7763.74	9145.33	17112	30	0.144163	35.6239
31	9349.64	10627.9	19904.9	31	0.126324	-8.89116
32	11225.6	12727	23867.8	32	0.105366	-9.0698

Figure A.2: Matrix of the detector to detector mean delay times (all cells listed in ns)

	0	1	2	3	4	5	6	7	8	9	10	11	12	13	14	15	16	17	18	19	20	21	22	23	24	25	26	27	28	29	30	31
0		73.71	103.5	103.8	141.8	41.42	123.1	44.88	172	109.6	35.25	160.1	62.37	257	138.7	159.4	161.6	147.8	141.4	124.9	175.9	204.3	156.3	88.77	117.7	182.6	152.6	154.1	132.5	86.44	204.7	133.9
1			48.36	47.75	76.49	-20.06	58.75	-14.37	79.19	85.69	-26.18	81.37	31.41	67.79	53.63	26.87	64.96	85.42	75.08	71.49	130.3	102.9	118.3	34.11	72.07	92.94	131.9	90.57	90.03	10.78	112.5	72.15
2				13.28	58.62	-52.91	23.36	-46.13	54.76	42.09	-95.92	48.98	-14.85	72.2	5.3	50.17	93.33	39.8	33.06	27.68	65.62	42.82	84.53	-5.12	27.01	54.36	67.36	39.36	56.13	-38.68	69.85	32.21
3					48.47	-67.88	27.28	-66.19	45.81	36.78	-87.9	52.74	-21.37	80.43	-17.17	-3.3	63.81	49.47	37.49	23.05	83.12	58.52	54.94	-7.59	51.98	49.1	89.35	26.37	24.33	-29.95	57.51	23.9
4						-104.1	-15.88	-94.23	4.79	9.23	-117.9	1.37	-71.3	18.83	-51.68	-4.72	19.27	-32.03	-31.82	-16.24	4.73	30.44	47.32	-110.4	-4.42	37.46	8.893	-2.14	-17.47	-74.97	15.66	-55.21
5							83.13	20.22	107.3	110.2	-9.07	102	40.56	112.1	84.49	101.5	86.85	109.9	102	77.94	146.5	108.9	166.2	50.79	87.52	131.2	135.8	105.9	101.5	33.79	120.9	84.7
6								-84.09	37.68	31.19	-75.87	31.49	-35.09	25.87	-19.76	-22.17	31.57	24.97	8.63	3.33	68.19	32.98	53.68	-24.48	7.47	34.8	73.53	1.08	-20.42	-45.43	36.89	16.19
7									95.18	93.22	-27.93	97.13	26.85	86.21	66.25	85.93	119.4	113.8	70.65	113.8	110.3	122.7	130.5	29.86	89.74	117.7	141.1	92.95	100.6	48.39	118.4	73.53
8										-11.84	-131.4	5.97	-62.04	6.07	-32.39	-39.5	24.32	-9.37	-13.38	-24.85	-1.2	19.02	36.45	-47.63	-22.08	9.44	34.06	13.85	-1.69	-72.56	20.89	-24.88
9											93.19	8.58	-55.73	-7.06	-31.76	-11.02	15.53	1.7	0.13	-20.03	30.32	14.61	43.25	-49.21	-9.73	24.13	53.93	-12.14	4.07	-67.08	15.32	-9.345
10												93.19	50.39	124.7	71.93	92.91	117.5	114.5	88.33	98.18	142.2	146.9	169.3	46.97	113.4	137.3	131	13.85	105	43.09	165.6	54.76
11													-63.24	1.54	-36.87	-52.46	-53.27	-41.68	-12.45	-23.61	32.56	6.89	26.07	-51.3	-21.61	13.5	46.36	4.746	0.5833	-83.37	20.8	-12.5
12														76.56	18.74	87.99	52.8	57.63	35.7	35.45	59.49	102.1	105.8	10	41.17	55.34	91.22	61.07	78.64	1.73	79.67	53.69
13															-40.91	-33.89	1.08	-0.13	-20.4	-18.24	25.76	41.02	46.29	-69.54	-45.18	15.67	3.608	-30.38	-24.46	-79.36	27.48	-1.02
14																-4.04	35.31	24.39	18.38	2.53	83.93	52.98	59.32	-23.2	20.32	65.56	69	45.27	39.44	-22.53	55.21	27.25
15																	37.64	29.42	-0.59	-61.43	45.49	53.87	75.72	-99.61	-14.7	51.95	48.48	23.43	10.37	-100.6	56.75	73.66
16																		2.78	-9.54	-39.22	15.51	16.81	48.32	-61.22	13.21	19.83	29.5	-3.883	-36.03	-86.8	-0.29	-58.27
17																			-24.77	-13.27	21.73	21.11	36.42	-40.01	-1.593	23.89	22.99	-0.14	-9.3	-91.96	12.03	-9.02
18																				4.09	35.2	31.45	52.17	-36.43	13.04	28.48	64.08	34.77	26.2	-91.35	39.07	19.32
19																					19.79	4.09	50.22	-49.76	6.7	33.79	58.19	-24.66	-8.54	1.73	54.57	11.24
20																						-1.373	55.31	-85.4	-14.38	-1.85	62.41	-18.24	-44.6	-79.36	47.41	13.27
21																							5.61	-73.22	-24.08	2.32	31.9	-32.92	-26.01	-22.53	7.31	-30.38
22																								-83.86	-53.5	-21.35	22.59	74.9	-56.24	-100.6	-22.22	-55.78
23																									39.16	86.3	105.4	-26.17	69.32	-131.9	72.49	41.58
24																										34.49	67.97	-20.37	-7.02	6.29	29.99	6.81
25																											42.64	-37.25	-51.55	-46.05	5.03	-11.49
26																												-20.03	-73.11	-93.56	-41.62	-55.7
27																													-20.03	-117.9	47.5	5.35
28																														-62.18	90.81	-18.89
29																															47.5	70.65
30																																-24.42
31																																

Figure A.3: Matrix of the counts detected by each of the CsI detectors during ^{60}Co collection

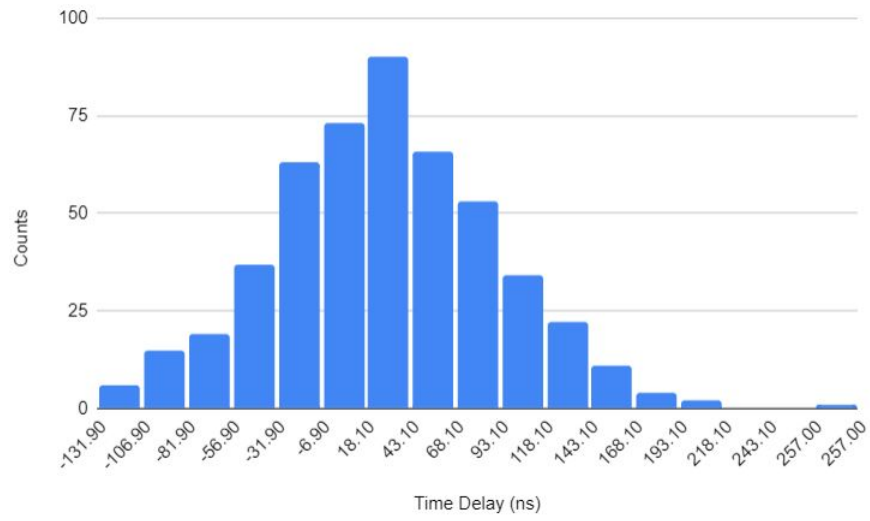|	0	1	2	3	4	5	6	7	8	9	10	11	12	13	14	15	16	17	18	19	20	21	22	23	24	25	26	27	28	29	30	31
0	73.71	103.5	103.8	141.8	41.42	123.1	44.88	172	109.6	35.25	160.1	62.37	257	138.7	159.4	161.6	147.8	141.4	124.9	175.9	204.3	156.3	88.77	117.7	182.6	152.6	154.1	132.5	86.44	204.7		133.9
1		48.36	47.75	76.49	-20.06	58.75	-14.37	79.19	85.69	-26.18	81.37	31.41	67.79	53.63	26.87	64.96	85.42	75.08	71.49	130.3	102.9	118.3	34.11	72.07	92.94	131.9	90.57	90.03	10.78	112.5		72.15
2			13.28	58.62	-52.91	23.36	-46.13	54.76	42.09	-95.92	48.98	-14.85	72.2	5.3	50.17	93.33	39.8	33.06	27.68	65.62	42.82	84.53	-5.12	27.01	54.36	67.36	39.36	56.13	-38.68	69.85		32.21
3				48.47	-67.88	27.28	-66.19	45.81	36.78	-87.9	52.74	-21.37	80.43	-17.17	-3.3	63.81	49.47	37.49	23.05	83.12	58.52	54.94	-7.59	51.98	49.1	89.35	26.37	24.33	-29.95	57.51		23.9
4					-104.1	-15.88	-94.23	4.79	9.23	-117.9	1.37	-71.3	18.83	-51.68	-4.72	19.27	-32.03	-31.82	-16.24	4.73	30.44	47.32	-110.4	-4.42	37.46	8.893	-2.14	-17.47	-74.97	15.66		-55.21
5						83.13	20.22	107.3	110.2	-9.07	102	40.56	112.1	84.49	101.5	86.85	109.9	102	77.94	146.5	108.9	166.2	50.79	87.52	131.2	135.8	105.9	101.5	33.79	120.9		84.7
6							-84.09	37.68	31.19	-75.87	31.49	-35.09	25.87	-19.76	-22.17	31.57	24.97	8.63	3.33	68.19	32.98	53.68	-24.48	7.47	34.8	73.53	1.08	-20.42	-45.43	36.89		16.19
7								95.18	93.22	-27.93	97.13	26.85	86.21	66.25	85.93	119.4	113.8	70.65	66.41	110.3	122.7	130.5	29.86	89.74	111.7	141.1	92.95	100.6	48.39	118.4		73.53
8									-11.84	93.22	5.97	-62.04	6.07	-32.39	-39.5	24.32	-9.37	-13.38	-24.85	-1.2	14.61	36.45	-47.63	-22.08	9.44	34.06	13.85	-1.69	-72.56	20.89		-24.88
9										-131.4	8.58	-55.73	-7.06	-31.76	-11.02	15.53	1.7	0.13	98.18	30.32	146.9	43.25	-49.21	-9.73	24.13	53.93	-12.14	4.07	-67.08	15.32		-9.345
10											93.19	50.39	124.7	71.93	92.91	117.5	114.5	88.33	-23.61	142.2	6.89	169.3	46.97	113.4	137.3	131	112.8	105	43.09	165.6		54.76
11												-63.24	1.54	-36.87	-52.46	-53.27	-41.68	-12.45	35.45	32.56	102.1	26.07	-51.3	-21.61	13.5	46.36	4.746	0.5833	-83.37	20.8		-12.5
12													76.56	18.74	87.99	52.8	57.63	35.7	-18.24	59.49	41.02	105.8	10	41.17	55.34	91.22	61.07	78.64	1.73	79.67		53.69
13															-33.89	1.08	-0.13	-20.4	2.53	25.76	52.98	46.29	-69.54	-45.18	15.67	3.608	-30.38	-24.46	-79.36	27.48		-1.02
14															-40.91	35.31	24.39	18.38	-61.43	83.93	53.87	59.32	-23.2	20.32	65.56	69	45.27	39.44	-22.53	55.21		27.25
15																37.64	29.42	-0.59	-39.22	45.49	16.81	75.72	-99.61	-14.7	51.95	48.48	23.43	10.37	-100.6	56.75		73.66
16																	2.78	-9.54	-13.27	15.51	21.11	48.32	-61.22	13.21	19.83	29.5	-3.83	-36.03	-86.8	-0.29		-58.27
17																		-24.77		21.73	31.45	36.42	-40.01	-1.593	23.89	22.99	-0.14	-9.3	-91.96	12.03		-9.02
18																			4.09	-13.27	33.94	52.17	-36.43	13.04	28.48	64.08	26.2	26.2	-9.3	39.07		19.32
19																				19.79		50.22	-49.76	6.7	33.79	28.48	34.77	-8.54	26.74	54.57		11.24
20																					-1.373	55.31	-85.4	-14.38	-1.85	33.79	74.9	-44.6	-48.13	47.41		13.27
21																						5.61	-73.22	-24.08	2.32	31.9	-26.01	-60.67	7.31		-30.38
22																							-83.86	-53.5	-21.35	22.59	-56.24	-91.35	-22.22		-55.78
23																								39.16	86.3	105.4	69.32	-131.9	72.49		41.58
24																									34.49	67.97	-7.02	6.29	29.99		6.81
25																										42.64	-51.55	-93.56	5.03		-11.49
26																												-73.11	-117.9	-41.62		5.35
27																												-20.03		47.5		-55.7
28																														90.81		-18.89
29																																70.65
30																																-24.42
31																																

Figure A.4: Time delay histogram